

Experimental studies of the cross-excitation instability in a relativistic backward wave oscillator

F. Hegeler, M. Partridge, E. Schamiloglu¹, C.T. Abdallah, and N. Islam

Department of Electrical and Computer Engineering
University of New Mexico
Albuquerque, NM 87131

ABSTRACT

Our group first reported the operation of a relativistic backward wave oscillator (BWO) in the so-called “cross-excitation” regime in 1998. This instability, whose general properties were predicted earlier through numerical studies, was a consequence of using a particularly shallow rippled-wall waveguide (slow wave structure – SWS) that was installed in the experiment to diagnose pulse shortening in a long pulse electron beam-driven high power microwave (HPM) source. This particular SWS was required to accommodate laser interferometry measurements during the course of microwave generation. Since those early experiments we have further studied this regime in greater detail using two different SWS lengths. We have invoked time-frequency analysis, the smoothed-pseudo Wigner-Ville distribution in particular, to interpret the heterodyned signals of the radiated power measurements. These recent results are consistent with earlier theoretical predictions for the onset, voltage scaling, and general behavior for this instability. This paper presents data for a relativistic BWO operating in the single frequency regime for two axial modes, operating in the cross-excitation regime, and discusses the interpretation of the data, as well as the methodology used for its analysis. Although operation in the cross-excitation regime is typically avoided due to its poorer efficiency, we discuss how it may be exploited in HPM effects studies.

Keywords: relativistic BWO, high power microwaves, joint time-frequency analysis, cross-excitation instability, mode competition

1. INTRODUCTION

Since the 1970’s [1] there has been continuous interest in the development of high peak power microwave (HPM) devices driven by intense relativistic electron beams, beginning with the backward wave oscillator (BWO). Kurilko *et al.* [2] presented the first comprehensive theoretical analysis describing the operation of an intense relativistic electron beam-driven BWO. This analysis was later expanded by Sweigle and colleagues [3-4]. More recently, Levush *et al.* [5] developed a theory of BWO operation that incorporates finite length effects of the slow wave structure (SWS), in particular the effects of reflections of the microwaves at both ends of the device. Subsequent experiments and electromagnetic particle-in-cell (PIC) simulations by Moreland *et al.* [6] elucidated the role of finite length effects on both microwave frequency and generation efficiency. In their work, Moreland and colleagues noted that a phase shift between the first and zeroth spatial harmonics plays a critical role in determining the operating characteristics of a finite length BWO. Vlasov *et al.* [7] further studied this effect using a nonlinear model, and Nusinovich and Bliokh [8] developed a theory describing the mode interaction with strong end reflections.

In their analysis, Levush and colleagues describe several operating regimes of intense relativistic electron beam-driven BWO’s that strongly depend on the length of the beam-microwave interaction region (*i.e.*, the number of ripple periods comprising the SWS) and the reflection coefficients at the ends. By sufficiently varying either the reflection coefficients or the beam parameters, mode competition can occur whereby two frequencies can be generated simultaneously. In particular, three parameters are considered in detail: a normalized length k_*L , the ratio of the beam current to start-oscillation current $\chi = I_{\text{beam}} / I_{\text{st}}$, and the reflection coefficient R at the downstream end of the SWS (the reflection coefficient at the upstream end is assumed to be 1.0 at the cutoff waveguide inlet to the electrodynamic system). Regarding the normalized length, k_* is the resonant wave number, defined by the intersection of the doppler line with the cold SWS dispersion curve, and L is the physical length of the SWS. For a fixed length SWS, the normalized length can still vary through changes in beam energy (caused in turn by changes in diode voltage) that will affect k_* . Figure 1 shows the dispersion relation of the UNM BWO

¹ Correspondence: edl@ece.unm.edu. Paper presented at SPIE 2000, Orlando, FL. April 2000.

with a uniform SWS at the TM_{01} mode. As the beam voltage decreases, the resonant wave number k_* increases in order to preserve the intersection of the beam structure dispersion relation.

The value of k_* determines whether the BWO operates in a steady, single frequency regime or in a multi-frequency regime characterized by instabilities that result from over-bunching of the electron beam (see Figure 2). An additional regime exists where the start current and gain of one mode is modified by the presence of another saturated mode, enabling the second mode to compete with the first. Levush and his colleagues refer to this regime as the “cross-excitation instability” regime. If the amplitudes of the two modes are approximately the same, the total power output and efficiency of the BWO are essentially unchanged, but no single-frequency equilibrium is achieved. If the second mode has a considerably larger amplitude, the first mode will be suppressed and a noticeable jump in efficiency, power output, and frequency will occur as the second mode reaches saturation. (The nonlinear excitation of parasitic modes in the context of gyrotrons was discussed early on by Nusinovich [9], and the essence of the cross-excitation instability can be understood in the context of the framework he describes.)

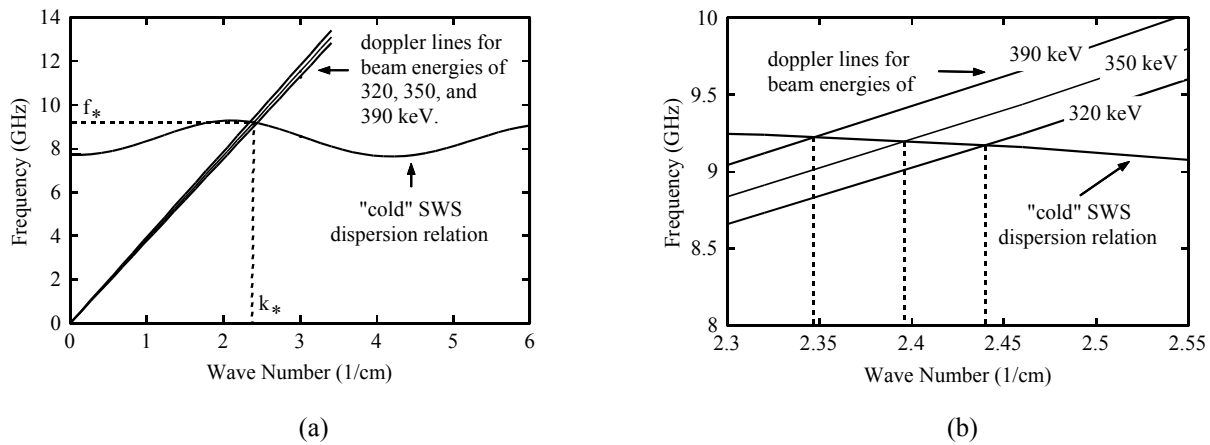


Figure 1. The “cold” SWS dispersion relation of the UNM BWO at the TM_{01} mode. The resonant wave number k_* is defined by the intersection of the doppler line with the cold SWS dispersion curve: (a) general overview and (b) magnified view.

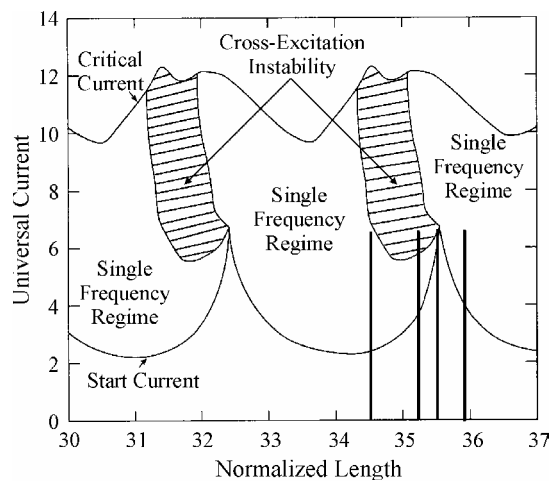


Figure 2. Regions of BWO operation in the universal current-normalized length parameter space for a reflection coefficient of 0.7 at the downstream end of the SWS. The region of cross-excitation will widen with a larger reflection coefficient. The vertical lines at the normalized lengths of 34.5, 35.2, 35.5, and 35.9 mark the positions of the experimental regimes with a 10-period SWS, as shown as in Figures 13, 9, 10, and 12, respectively. (The universal start current for this BWO can only be estimated, and thus, the exact value is unknown.) An overbunch instability regime exists in the area above the critical current.

This paper presents results from the experimental observation of a long pulse relativistic BWO operating in the single frequency regime at two different axial modes, as well as operating in the cross-excitation regime. The cross-excitation instability was alluded to as one of several mechanisms that could explain a frequency change during a power dip in an earlier BWO experiment [10], resulting in pulse shortening. The first observation of this instability where the appropriate scaling was demonstrated was reported by us in Ref. [11]. Since then, significant progress has been made in both the analysis of the measurements and in controllably operating in and out of this regime. Time-frequency analysis has proven to be invaluable in characterizing operation in the cross-excitation regime, both for a 10- and 12-period SWS. We conclude this paper by discussing how this instability can be exploited for HPM effects studies.

2. EXPERIMENTAL SET-UP AND DATA ANALYSIS

The experimental results presented in this paper were conducted using the University of New Mexico (UNM) long-pulse BWO experiment, whose cross section is shown schematically in Figure 3. An electron beam is emitted from an annular knife-edge graphite cathode, and is guided by a magnetic field of 2 T through various SWS configurations onto a beam dump. All data presented in this paper have been obtained for peak cathode voltages ranging from 320-500 kV, beam currents ranging from 1-2 kA, and an anode-cathode (*A-K*) gap spacing of 2.5 cm. The generated microwaves are radiated using a conical horn antenna 12.7 cm in diameter, covered with a 0.25 mm-thick Mylar window to maintain the vacuum-to-air interface. (More complete information on the accelerator and the general experimental set-up is available in Ref. [12].)

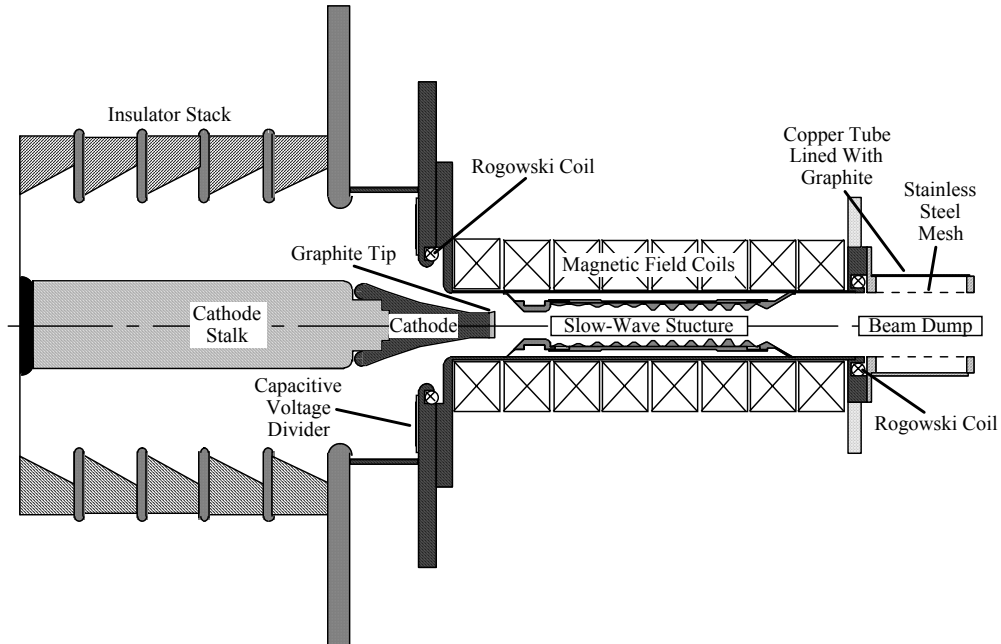


Figure 3. Cross-sectional diagram of the long-pulse backward-wave oscillator.

The SWS is made from a modular construction in which each ripple is machined out of a ring of stainless steel and then slid into a tube holding them in place. For operation in the cross-excitation regime, either a 10- or 12-period uniform amplitude structure was used, as shown in Figure 4. This structure had been installed for a previous experiment to accommodate laser interferometry measurements during the course of microwave generation [13]. Each ring of the SWS has a width (ripple period) of 14.7 mm, a mean radius of 14.64 mm, and a ripple amplitude of 1.86 mm, and a minor inner diameter of 25.56 mm. The cutoff neck inlet to the electrodynamic structure has an inner diameter of 23 mm, and the annular electron beam is positioned between a radius of 9 mm and 11.5 mm [12]. (Note that the particularly shallow rippled-wall SWS is not optimized for maximum microwave generation efficiency.) The annular beam halos scrapes along the inner wall of the cutoff neck, producing plasma, which is one of the leading causes for pulse shortening. A detailed description of these measurements is given in reference [13]. Since this beam scraping occurs during operation in both the single frequency and cross-excitation regimes, it is not relevant to the cross-excitation instability's onset.

Figure 5 presents the set-up used for microwave power and frequency measurements. The detector antenna, a short, open-ended section of WR-90 waveguide, is placed in the far-field region of the TM_{01} mode radiation pattern at an angle of 25°

from the centerline of the conical horn antenna. The BWO radiates in the TM_{01} mode for both single frequency and cross-excitation regimes. A directional coupler, semi-rigid coaxial cable, and coaxial attenuators reduce the microwave signal received by the detector antenna. The signal from the detector antenna is split into two signals using a power divider, one path which enters a crystal detector for power measurement, and the other heterodyned with a known local oscillator (LO) signal for frequency determination. In order to determine the microwave frequency more precisely, initial frequency measurements were taken using various LO frequencies. The attenuation of the microwave diagnostic components were calibrated using an HP8720D network analyzer, and the measurements are transferred to a personal computer using LabVIEW®, taking into account the different attenuation values for various frequencies. Typical waveforms of the cathode voltage and beam current during microwave generation are given in Figure 6. Since microwaves are generated during the rising part of the voltage pulse, the resonant wave number k_* (see Figure 1) is calculated using an average beam voltage. The current and voltage pulse shapes presented in Figure 6 are comparable for both single frequency and cross-excitation cases; the amplitudes of the voltage and current pulse are different.

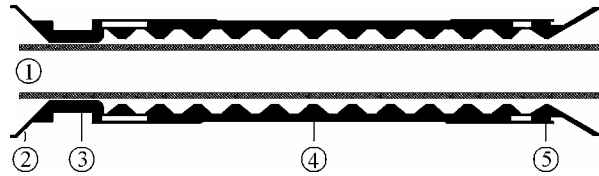


Figure 4. Configuration of the uniform slow-wave structure: 1) annular electron beam, 2) anode of the A-K gap, 3) cutoff neck, 4) periodic ripple-walled structure, and 5) impedance matching ring.

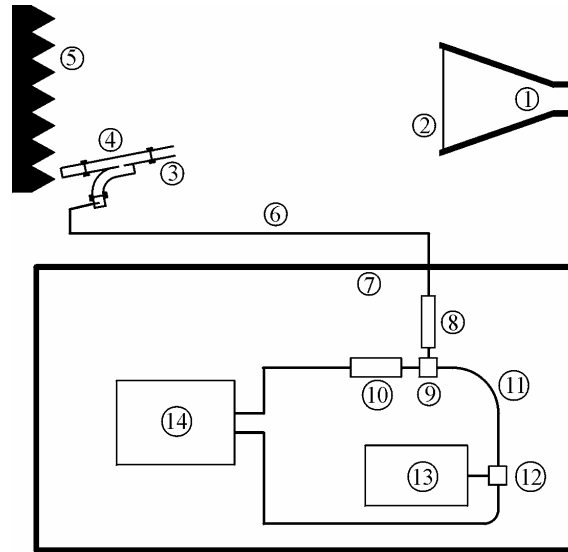


Figure 5. Microwave power and frequency diagnostic set-up for both the single frequency and cross-excitation regime: 1) conical horn antenna, 2) Mylar window, 3) open-ended X-band waveguide section, 4) 20 dB directional coupler with termination and X-band-to-coaxial adapter, 5) microwave absorber, 6) 17 m RG402/U (EZ141) semi-rigid coaxial cable, 7) shielded measurement room, 8) dc-to-12.4 GHz attenuators, 9) 6 dB power splitter, 10) 0.01-18 GHz crystal detector, 11) 0.4 m of RG402/U (EZ141) semirigid coaxial cable, 12) 8-12 GHz double balanced mixer, 13) local oscillator, and 14) 4 channel oscilloscope with a bandwidth of 1 GHz.

In our earlier studies, the radiated frequency was obtained from the heterodyned signal, which was separated into ten segments, and a simple Fourier transform of each segment was used to identify the major components. Although this technique identifies frequency changes over the entire microwave signal, it loses time information within the segment (or time window). In single frequency operation of the BWO this not a concern. However, if there is a significant change in the microwave frequency, this loss of time information can lead to a misinterpretation of the data. Therefore, joint time-frequency analysis (JTFA) is used to better understand the frequency signal. The use of JTFA in the HPM community was

first suggested by a group at the Israel Institute of Technology, Haifa [14]. We have tested various distributions for the JTFA to accurately display the temporal frequency measurements of the cross-excitation regime, which is the competition between (simultaneous presence of) two axial TM_{01} modes. The data obtained for this paper are analyzed using a smoothed-pseudo Wigner-Ville (SPWV) distribution.

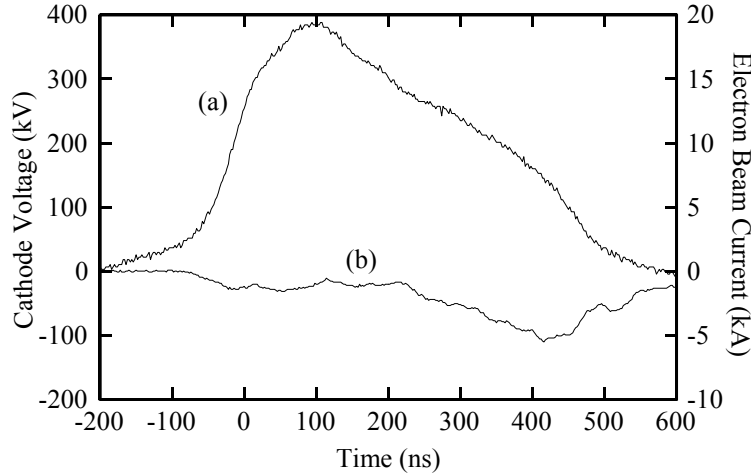


Figure 6. Typical waveforms of the cathode voltage and beam current. The microwave pulse starts at $t = 0$ for a duration of 50 to 80 ns. The average electron beam energy during microwave generation in this figure is 320 keV.

3. RESULTS AND DISCUSSION

The data and discussion presented below are based on about 100 shots taken with a 10- and 12-period uniform amplitude SWS at various beam voltages and currents. Out of these measurements, about 40 shots showed evidence of operation in the cross-excitation regime. Figure 7 presents data representative of operation in the cross-excitation regime for the 12-period SWS. The experimental parameters of this shot are a peak diode voltage ($V_{\text{diode, pk}}$) at the time of microwave generation of 400 kV and an average beam current ($I_{\text{beam, avg}}$) of 1.8 kA. The normalized length for this case is $k_*L = 41.3$. Note that microwaves are produced on the rising edge of the UNM long-pulse accelerator voltage, whereas the diode voltage at the start of the microwave pulse is approximately 90% of $V_{\text{diode, pk}}$. As can be seen from Figure 7, the radiated power initially rises to 22 MW at an output frequency of about 9.1 GHz. Approximately 5 ns after the peak power is reached, the power rapidly decreases as the second axial mode within the SWS begins to grow. It is observed that two modes beat simultaneously for a period of 5 ns, after which point the highest radiated power occurs at a frequency of about 9.5 GHz. This second mode results in a considerably more efficient beam-to-microwave energy conversion. Note that in all cross-excitation results the frequency of the initial mode is lower than the frequency of the second mode, since the diode voltage increases during the microwave pulse.

When the diode voltage is decreased to 350 kV, which also decreases the beam current to 1.2 kA, the normalized length k_*L is shifted to 42.3, and the ratio of the beam current to start-oscillation current χ is reduced compared to the previous case. In this single frequency regime (see Figure 8), the frequency varies slightly from 9.43 to 9.5 GHz due to an increase of the diode voltage during microwave generation. The maximum radiated power is less than the data shown in Figure 7 since the beam energy is reduced. In addition, it is evident from Figures 7 and 8 that the maximum beam-to-microwave energy conversion efficiency in single mode operation is greater than in the cross-excitation regime.

Operation in the cross-excitation regime is also observed when the BWO is fitted with a shorter SWS that consists of 10 periods. Figures 9-11 present a variety of data with similar normalized lengths k_*L of 35.2 to 35.5. With slight variations of the beam voltage and current parameters, large changes in the operation in the cross-excitation regime are evident. Figure 9 presents data in the cross-excitation regime where the two axial modes have similar maximum power levels. Figure 10 presents data in the cross-excitation regime where the initial axial mode has a lower power level compared with the second axial mode, and Figure 11 illustrates the opposite case. Although the universal start current for this BWO can only be estimated, and thus, a direct comparison with the original modeling results is not possible, the experimental data for the 10-

period SWS at the normalized lengths k_*L are consistent with the position of the cross-excitation instability region (see Figure 2). Single mode operation with the 10-period SWS is obtained when the diode voltage is either decreased or increased compared to the value of $V_{\text{diode,pk}}$ corresponding to operation in the cross-excitation regime. Lowering the diode voltage will lead to single frequency operation at the lower axial mode (see Figure 12), and increasing the diode voltage will lead to single frequency operation at the higher axial mode (see Figure 13). Pulse shortening due to cross-excitation has not been observed. On average, the microwave pulse duration in the cross-excitation regime is equal to or slightly larger than for the case with a single frequency. Since the power amplitude decreases during the simultaneous beating of the two axial modes in the cross-excitation regime, the microwave energy for the single frequency case is greater.

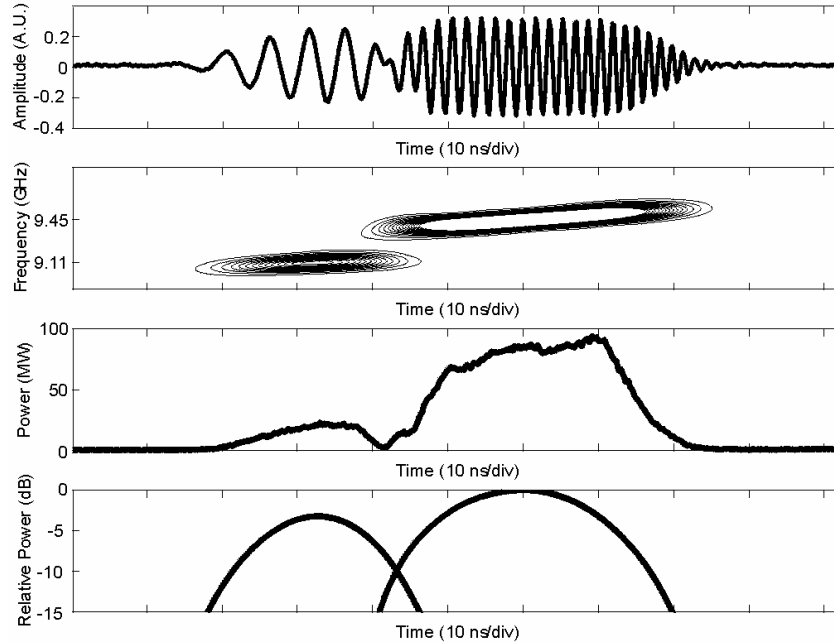


Figure 7. Evidence of the cross-excitation instability. Top: Heterodyned frequency signal with a LO frequency of 8.9 GHz. Second from top: SPWV time-frequency distribution. Second from bottom: Microwave power. Bottom: Relative power in dB at the two mean frequencies of 9.11 and 9.45 GHz ($V_{\text{diode,pk}} = 400$ kV, $I_{\text{b,avg}} = 1.8$ kA, and $k_*L = 41.3$, using a 12-period SWS).

Future work will study the factors that contribute to the temporal coexistence of the modes, yielding some insight into mode saturation and/or electron trapping. Although operation in the cross-excitation regime is less efficient than single frequency operation, it may prove useful to future HPM effects studies. This is discussed in the next section.

4. USE OF CROSS-EXCITATION REGIME OPERATION FOR HPM EFFECTS STUDIES

The interaction of electronic systems and devices with an HPM beam at a distance may result in the degradation, behavior modification, or simple failure of the system. The end result would be similar to the response of electronics to nuclear radiation, where device catastrophic failures, memory upset, latch-up and degradation of threshold voltage have been reported [15]. For HPM beam-system interactions various parameters need to be analyzed. These include the effects of (i) the source amplitude, (ii) transfer function of the radiating antenna, (iii) the propagation path, (iv) the response of the outer surface and, (v) the response of the system interior. The overall effect at any point then will be the result of the effects of these parameters. Analysis of such coupling between the source and the system is usually defined through a parameter called the receiving cross section, which is defined as a function of such parameters as the directivity gain, radiated power density, impedance matching factor, and the Ohmic efficiency [16]. Alternately, a system's tolerance to HPM can also be characterized in terms of the power density, energy, or the fluence of the incident beam. Another approach to HPM beam-system analysis is to find the effects of a given peak field strength on the device/system in consideration. For each of these examples, there are scenarios where an HPM beam comprising two distinct frequencies may prove advantageous.

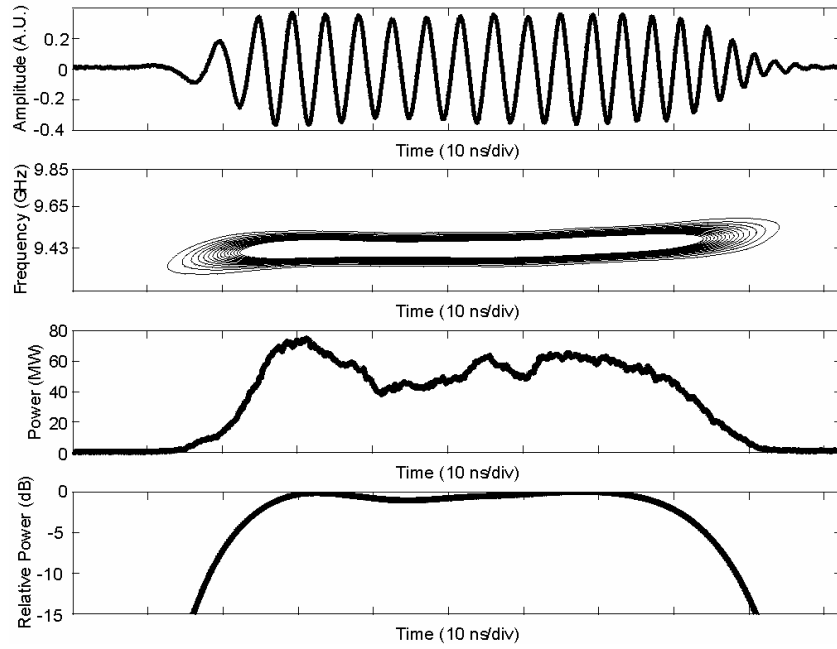


Figure 8. Data illustrating single mode operation. Top: Heterodyned frequency signal with a LO frequency of 8.9 GHz. Second from top: SPWV time-frequency distribution. Second from bottom: Microwave power. Bottom: Relative power in dB at the mean frequency of 9.43 GHz ($V_{\text{diode,pk}} = 350$ kV, $I_{\text{b,avg}} = 1.2$ kA, and $k_*L = 42.3$, using a 12-period SWS).

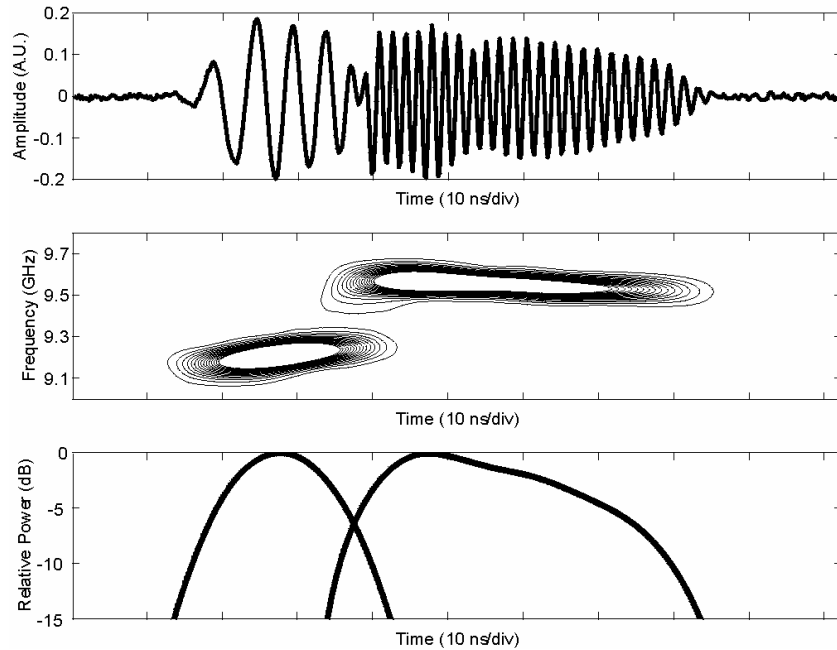


Figure 9. Cross-excitation instability measured with a 10-period SWS. Top: Heterodyned frequency signal with a LO frequency of 9 GHz. Middle: SPWV time-frequency distribution. Bottom: Relative power in dB at the two mean frequencies of 9.21 and 9.57 GHz ($V_{\text{diode,pk}} = 350$ kV, $I_{\text{b,avg}} = 1.2$ kA, and $k_*L = 35.2$).

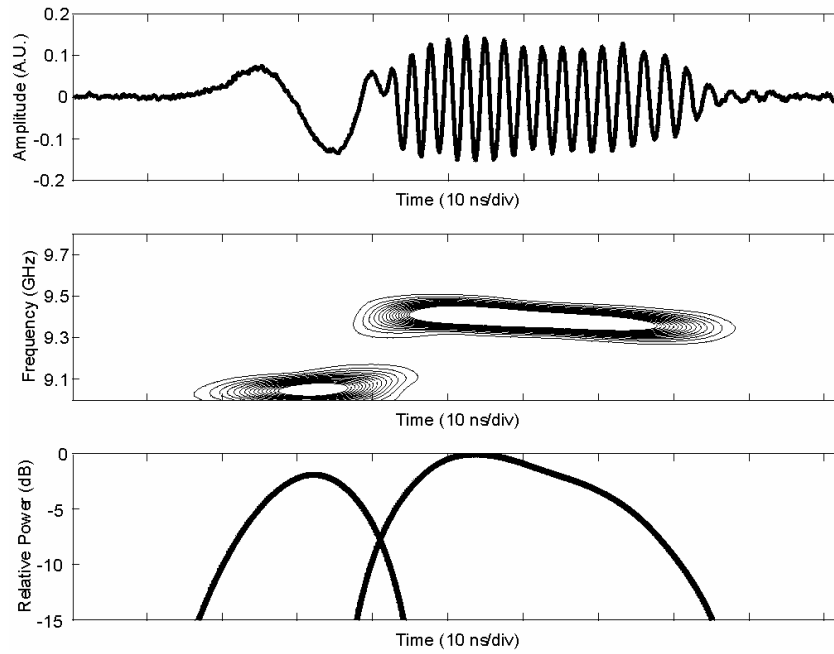


Figure 10. Cross-excitation instability measured with a 10-period SWS. Top: Heterodyned frequency signal with a LO frequency of 9 GHz. Middle: SPWV time-frequency distribution. Bottom: Relative power in dB at the two mean frequencies of 9.05 and 9.41 GHz ($V_{\text{diode,pk}} = 340$ kV, $I_{\text{b,avg}} = 1.2$ kA, and $k_*L = 35.5$).

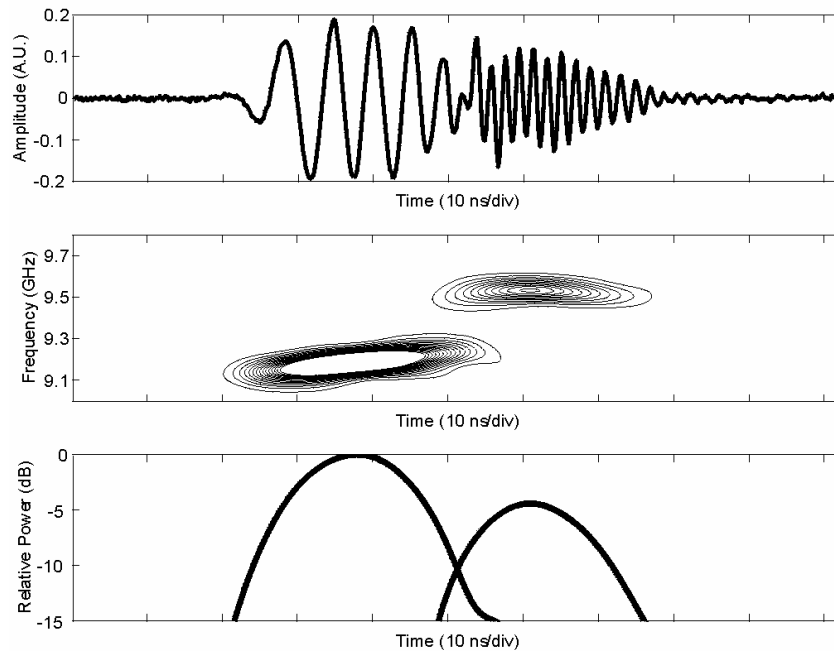


Figure 11. Cross-excitation instability measured with a 10-period SWS. Top: Heterodyned frequency signal with a LO frequency of 9 GHz. Middle: SPWV time-frequency distribution. Bottom: Relative power in dB at the two mean frequencies of 9.19 and 9.54 GHz ($V_{\text{diode,pk}} = 340$ kV, $I_{\text{b,avg}} = 1.1$ kA, and $k_*L = 35.5$).

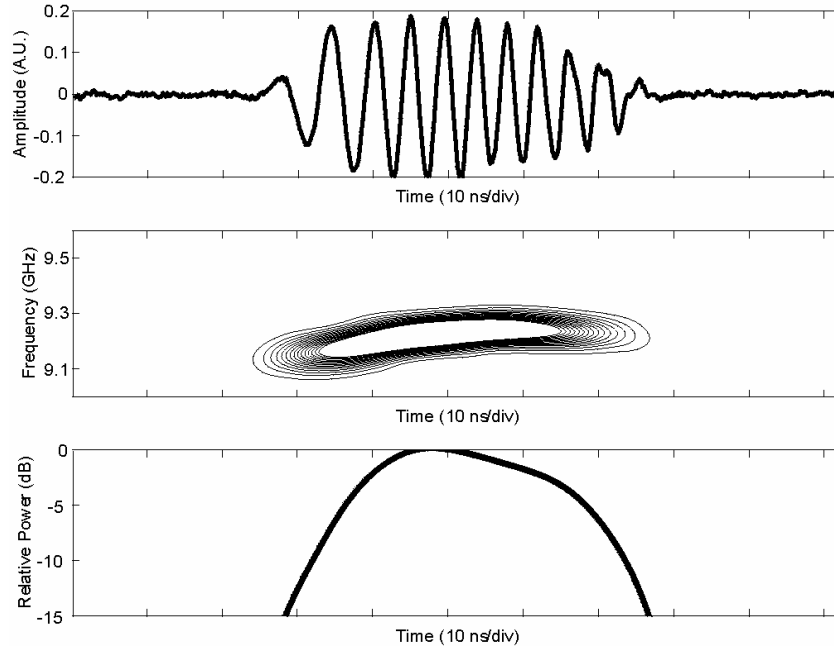


Figure 12. Low frequency single mode operation measured with a 10-period SWS. Top: Heterodyned frequency signal with a LO frequency of 9 GHz. Middle: SPWV time-frequency distribution. Bottom: Relative power in dB at the mean frequency of 9.2 GHz ($V_{\text{diode,pk}} = 320$ kV, $I_{\text{b,avg}} = 1.0$ kA, and $k_*L = 35.9$).

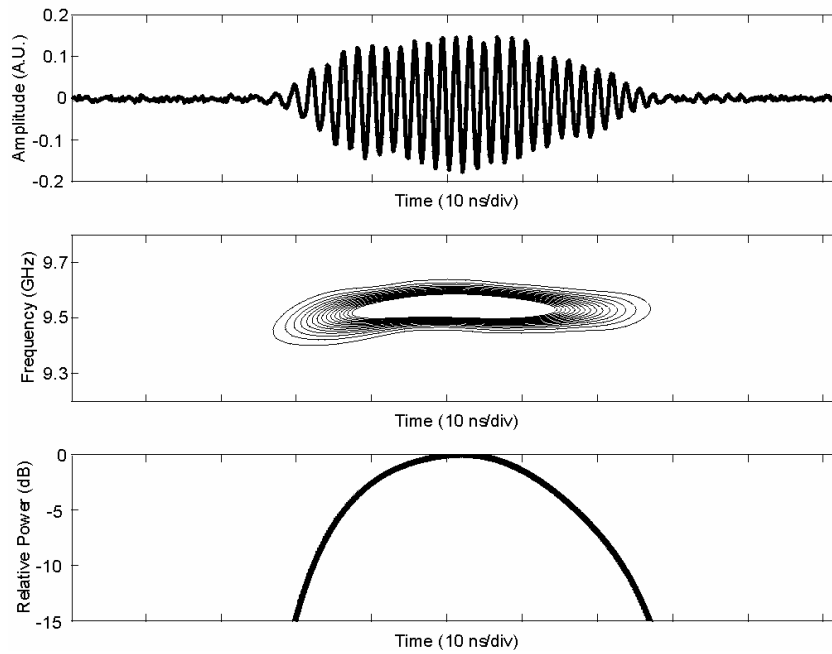


Figure 13. High frequency, single mode operation measured with a 10-period SWS. Top: Heterodyned frequency signal with a LO frequency of 9 GHz. Middle: SPWV time-frequency distribution. Bottom: Relative power in dB at the mean frequency of 9.5 GHz ($V_{\text{diode,pk}} = 390$ kV, $I_{\text{b,avg}} = 1.7$ kA, and $k_*L = 34.5$).

For simulation studies related to the tolerance of electrical systems to high power microwaves, a number of areas are being considered. These are heating effects including thermal damage, charge generation at a node, and electrical coupling through rectification and intermodulation. The overall damage mechanism will depend on the incident microwave power density, energy, fluence, or the peak field strength. As a result, the device may experience rectification where the signal, entering through interconnects and/or power cables, may be propagated to a nonlinear device such as the detector of an AM radio or the bipolar junction transistor input to a digital gate. The resulting signal may pass as a “true” signal, thereby upsetting data transmission and storage. Besides rectification, the device may go into a latch-up mode, induced from a parasitic transistor similar to those common to multi-junction SCR-type switches or CMOS circuits. Burnout of a CMOS structure may also result in circuit failure. Finally, thermal effects may also include local heating and secondary breakdown.

Operation of a relativistic BWO in the cross-excitation regime leads to the radiation of two distinct frequencies with an overlap in time of several nanoseconds. Simulations of the effect of this output on devices is presently being studied. The simulation tool we have available is the SILVACO [17] TCAD tool for semiconductor studies. This is a comprehensive tool that can perform semiconductor process, device, and circuit simulations using a common interface. Using this TCAD tool, a device can be “virtually fabricated” using the ATHENA module, and then can be a part of a circuit where the response of the circuit to changing device parameters can be analyzed. The code includes numerous models and parameters that can be defined for any specific situation to obtain the best results possible. The code, with a main interface (ATLAS) and other interactive tools, provides for a 2- and 3-D semiconductor device simulation that also includes thin film transistors (TFT), quantum devices, heterostructures, and power devices. In addition to the drift-diffusion model, one can study such “non-local” effects as velocity overshoot, reduced energy-dependent impact ionization, *etc.* using the energy balance model wherein such transport parameters as mobility and impact ionization become functions of the local carrier temperature rather than the local electric field.

The circuit simulation module includes lossy transmission line elements, all known device models, polynomial capacitors, temperature-dependent resistors and capacitors, and a variety of voltage and current sources. Circuit simulations can be configured for dc, ac, transient, and frequency-noise analysis. Finally, the code also has a provision to incorporate user-defined functions through a C-interpreter. This interpreter can be used in a variety of ways, such as to input changes in carrier mobilities, generation rate, *etc.* The simulation provides a self-consistent solution of Poisson’s equation and the continuity equation, describing the variation in electrostatic potential with local charge densities. The evolution of electron and hole densities due to transport, generation, recombination, *etc.* can be plotted for analysis.

As noted earlier, the code provides for the generation of carriers through out the device or at a particular node. This is accomplished through the C-interpreter function addressed through a pointer in the input file. The user can implement a generation function, which may change in intensity at a distance from the source. The effects are similar to radiation induced carrier generation that we have studied for sometime. Thus, a number of phenomena such as latch-up and CMOS burnout as a result of carrier generation due to microwave sources can be studied with the device module of the TCAD suite.

Bulk heating of the device is analyzed through absorption of radiation with associated changes in permittivity due to various molecular vibrational modes. The simulation device can then be divided into a number of regions with each region with a given permittivity value. In the absence of a (microwave) radiation source these values do not change. Following interaction with the source, microwave heating of the dielectric will occur, and surfaces interacting with incoming radiation may have a different permittivity value than other regions of the device. The resulting field, carrier concentration, and voltages as a result of this change will be extracted through simulation and analyzed in terms of the overall behavior of the device under microwave radiation.

Besides changes in permittivity, the heating of the contacts/interlinks during microwave interaction also results in a number of heat sources that may affect the device’s performance. The GIGA module accounts for lattice heat flow and general thermal environment through the incorporation of Wachutka’s thermodynamically rigorous model [18] of lattice heating that includes Joule heating, heating and cooling due to carrier generation and recombination, and the Peltier and Thomson effects. The dependence of material and transport parameters on lattice temperature and thermal environment is also included in the module. Thus, bipolar, MOS, IGBT, thyristors, and electrostatic discharge (ESD) protection devices can be studied with the module.

5. ACKNOWLEDGMENTS

This work is partly supported through a High Energy Microwave Devices Consortium funded by an AFOSR/DOD MURI grant and administered through Texas Tech University. The acquisition of some microwave diagnostic components was funded by an FY'99 AFOSR DURIP grant. This work is also partly supported by an AFOSR New World Vistas Grant.

6. REFERENCES

1. J. A. Nation, "On the coupling of an high-current relativistic electron beam to a slow wave structure," *Appl. Phys. Lett.*, vol. 17, pp. 491-494, 1970.
2. V. I. Kurilko, V. I. Kucherov, A. D. Ostrovskii, and Yu. V. Thach, "Stability of a relativistic electron beam in a periodic cylindrical waveguide," *Sov. Phys. Tech. Phys.*, vol. 24, pp. 1451-1454, 1979.
3. J. A. Swegle, J.W. Poukey, and G.T. Leifeste, "Backward-wave oscillators with rippled wall resonators: analytic theory and numerical-simulation," *Phys. Fluids*, vol. 28, pp. 2882-2894, 1985.
4. J. A. Swegle, "Approximate treatment near resonance of backward and traveling wave tubes in the compton regime," *Phys. Fluids*, vol. 28, pp. 3696-3702, 1985.
5. B. Levush, T. M. Antonsen, Jr., A. Bromborsky, W. R. Lou, and Y. Carmel, "Theory of relativistic backward-wave oscillators with end reflections," *IEEE Trans. Plasma Sci.*, vol. 20, pp. 263-280, 1992.
6. L. D. Moreland, E. Schamiloglu, R. W. Lemke, A. M. Roitman, S. D. Korovin, and V. V. Rostov, "Enhanced frequency agility of high-power relativistic backward wave oscillators," *IEEE Trans. Plasma Sci.*, vol. 24, pp. 852-858, 1996.
7. A. N. Vlasov, G. S. Nusinovich, and B. Levush, "Effect of the zero spatial harmonic in a slow electromagnetic-wave on operation of relativistic backward-wave oscillators," *Phys. Plasmas*, vol. 4, pp. 1402-1412, 1997.
8. G. S. Nusinovich and Yu. P. Bliokh, "Mode interaction in backward-wave oscillators with strong end reflections," *Phys. Plasmas*, vol. 7, pp. 1294-1301, 2000.
9. G. S. Nusinovich, "Mode interaction in gyrotrons," *Int. J. Electronics*, vol. 51, pp. 457-474, 1981.
10. J. A. Swegle, R. A. Anderson, J. F. Camacho, B.R. Poole, M. A. Rhodes, E. T. Rosenbury, and D. L. Shaeffer, "Scaling studies and time-resolved microwave measurements on a relativistic backward-wave oscillator," *IEEE Trans. Plasma Sci.*, vol. 21, pp. 714-724, 1993.
11. C. Grabowski, E. Schamiloglu, C. T. Abdallah, and F. Hegeler, "Observation of the cross-excitation instability in a relativistic backward wave oscillator," *Phys. Plasmas*, vol. 5, pp. 3490-3492, 1998.
12. C. Grabowski, J. M. Gahl, and E. Schamiloglu, "Electron-emission from slow-wave structure walls in a long-pulse, high-power backward-wave oscillator," *IEEE Trans. Plasma Sci.*, vol. 25, pp. 335-341, 1997.
13. F. Hegeler, C. Grabowski, and E. Schamiloglu, "Electron density measurements during microwave generation in a high power backward wave oscillator," *IEEE Trans. Plasma Sci.*, vol. 26, pp. 275-281, 1998.
14. I. Cohen, S. Raz, and D. Malah, "Time-frequency analysis and noise suppression with shift-invariant wavelet packets," *Proceedings Euroem'98*, Tel Aviv, Israel, June 14-19, 1998, appearing in *Ultra-Wideband, Short Pulse Electromagnetics 4*, Edited by Heyman *et al.*, Kluwer Academic/Plenum Publishers, NY, 1999, pp. 401-408.
15. G. C. Messenger and M. S. Ash, *The Effects of Radiation On Electronic Systems*, Van Nostrand, NY, Chapters 6 and 7, 1986.
16. R. K. Park and C. T. Tai, "Receiving Antennas," *Antenna Handbook*, Van Nostrand, NY, Chapter 7, 1988.
17. SILVACO International, 4701 Patrick Henry Drive, Santa Clara, CA, *ATLAS User's Manual*, www.silvaco.com.
18. G. K. Wachutka, "Rigorous thermodynamic treatment of heat generation in semiconductor device modeling," *IEEE Trans. Computer-Aided Design*, vol. 9, pp. 1141-1149, 1990.